

Characterization and Antibacterial Properties of Metal Borates Vectorized As Ceramic Glaze Additives

Osman Ağuş

Celal Bayar University: Manisa Celal Bayar Universitesi

Osman Arslan

Istanbul Sabahattin Zaim University: Istanbul Sabahattin Zaim Universitesi

YÜKSEL ABALI (✉ yuksel.abali@cbu.edu.tr)

Celal Bayar University: Manisa Celal Bayar Universitesi <https://orcid.org/0000-0002-4165-8656>

Research Article

Keywords: Antibacterial compound, silver borate, copper borate, zinc borate, nanoparticles, ceramic glaze, ceramic nanocomposite

Posted Date: March 10th, 2021

DOI: <https://doi.org/10.21203/rs.3.rs-294210/v1>

License:   This work is licensed under a Creative Commons Attribution 4.0 International License.

[Read Full License](#)

Abstract

Metal borate nanoparticles Silver (Ag), copper (Cu) and Zinc (Zn) were produced for a novel boron containing antibacterial ceramic applications. Different concentration, temperature, time parameters were varied for obtaining hierarchical metal borate embedded formulations. Synthesized nanostructures showed interesting crystalline and optical properties since temperature and concentration adjustments provided correlated shape and surface properties. Chemical analysis and crystallinity of both copper and silver formulations were defined using XRD and confirmed that temperature plays a deep role on the production of nanostructures. XPS analysis together with TEM investigations comprehensively provided all atomic compositions with their corresponding energy values in survey and high resolution region. Morphology and atomic purity was analyzed using EDX and SEM measurements revealed the morphological orientation of the nanostructures without other impurities. FT-IR and UV-Vis spectroscopy provided optical information about the obtained metal borate nanoparticles. Finally metal borate nanoparticles were utilized for 1x1 cm ceramic glazing samples for antibacterial applications. Silver borate nanoparticles were found to be more active in low concentrations than copper and zinc borate structures after the antibacterial test results were unveiled against to gram positive and gram negative microorganisms.

Introduction

Pathogens are very dangerous and effective on human health. Since pathogens are extremely stable on different environments pathogenic diseases have been increased in all around the world. While the diseases caused by the bacteria spread to a large extent among the societies, the use of antibacterial products is increasing day by day. The antibacterial effect is generally explained in three different mechanisms; ion release from the antibacterial agent or surface, light absorption and active photocatalytic or other methods for the cell wall destruction or again cell wall destruction by some chemicals such as quaternary ammonium salts (Fig. 1a). Figure 1b represents the general method for obtained silver borate, copper borate and zinc borate nanoparticles. New antibacterial products are emerging and spreading with the aim of preventing common infectious diseases. Therefore, the studies of compounds that do not have a toxic effect on health and have both antibacterial and antioxidant activities should increase rapidly [1–3]. Antibacterial materials have been widely used in many products such as pigment [4], water sterilization [5], food packaging [6], biomedicine [7, 8] and ceramics [9]. Therefore among other techniques, nano and even microstructures are useful materials in the micro/nanoscale range and they are very effective candidates utilized for the antibacterial applications. Micro and nano structures play intensive roles for antibiotic applications and removal of the pathogen infections [10], also drugs, sensors, artificial implants [11].

Micro/nano structures can have high surface area / volume ratios causing these structures having modified physical and chemical features when compared to bulk structures [12–13].

From this point, silver, copper, zinc and titanium dioxide structures were the actors for different anti-pathogenic surfaces [14–17].

Different nanostructures were utilized for antibacterial features, such as silver, magnesium(Mg), copper(Cu), aluminum(Al), Zinc (Zn) and their metal oxide structures [18]. Antibacterial nanoparticles, especially silver nanoparticles have wide usage in new technologies such as electronics, materials science and nano medicine [19, 20]. Silver NPs (AgNP) are used as antibacterial and antiviral materials in household appliances, aerogels, while Copper (Cu) NPs are used in antibacterial applications. Surface coating applications are widely utilized for antibacterial materials [21–23]. Antibacterial properties of silver and its compounds were established for centuries as silver ions, can exterminate a wide range of bacteria. Hence silver containing antibacterial materials are known for healing [24], pathogen related infections [25], urinary infections [26] and glaze applications [9]. Copper and copper based antibacterial have also started to be a popular material. Copper proposal for antibacterial glasses were also suggested with water cleaning applications [27].

As generally known metal borate nanostructures consist of Boron, Oxygen, Metal and hydrogen where connected to surface oxygen for their low coordination. There may also be water and hydroxyl groups in the crystal structure. Trihedral and tetrahedral boron oxygen structures are the basic structures of metal borates [28]. Copper borate compounds have examples like CuB_2O_4 , CuBO_2 , $\text{Cu}_3\text{B}_2\text{O}_6$, $\text{Cu}_2[\text{BO}(\text{OH})_2](\text{OH})_3$, $\text{Cu}_3\text{B}_6\text{O}_{12}\text{H}_2\text{O}$ and $\text{Cu}_3\text{B}_6\text{O}_{12}$. Fine-grained, blue and long-standing aqueous copper borates, such as $2\text{CuO}\cdot\text{B}_2\text{O}_3\cdot 3\text{H}_2\text{O}$ and $3\text{CuO}\cdot 2\text{B}_2\text{O}_3 \cdot n\text{H}_2\text{O}$ ($n = 5, 4, 2, 1$), have also been synthesized [29].

In this detailed investigation we have developed silver and copper borate nanostructures, conducted a detailed physical and chemical investigation for crystallinity, optical properties and surface features together with their antibacterial activities on ceramic surfaces. Results revealed that these borate nanostructures are the potential candidates for an industrial antibacterial application.

Materials And Methods

Borax ($\text{Na}_2\text{B}_4\text{O}_7\cdot 10\text{H}_2\text{O}$) (Merck), Silver Nitrate (AgNO_3) (Nalgene), Copper (II) Nitrate tri hydrate ($\text{Cu}(\text{NO}_3)_2\cdot 3\text{H}_2\text{O}$) (Merck) and Zinc nitrate hexahydrate ($\text{Zn}(\text{NO}_3)_2\cdot 6\text{H}_2\text{O}$) (Merck) were used for the mechanistic synthesis of metal borate nanoparticles. Chemicals are used as they were purchased. Silver nitrate (AgNO_3) and Sodiumboratedecahydrate ($\text{Na}_2\text{B}_4\text{O}_7\cdot 10\text{H}_2\text{O}$) have been used at $90\text{ }^\circ\text{C}$ by using the 2/1 proportions of Ag, Cu and Zn / $\text{Na}_2\text{B}_4\text{O}_7\cdot 10\text{H}_2\text{O}$. Additionally stirring speed was set to 400 rpm and reaction was conducted 2 hours respectively. Fig. 1b represents the general method for as-obtained metal borate nanoparticles. Produced nanoparticles were investigated after washing with EtOH, water and drying. Crystallinity was observed with XRD and particle morphology with statistical analysis conducted by SEM.

Methods

The X-ray diffraction (XRD) patterns of the metal borate nanoparticles was recorded at Philips X'Pert Pro X-Ray diffractometer, using CuK α radiation ($\lambda = 1.5406 \text{ \AA}$), 40 kV- 40mA, $2\theta/\theta$ scanning mode. Data was taken for the 2θ range of 10 to 80 degrees with a step of 0.0404 degree. The diffractograms were compared with the standard powder diffraction card of JCPDS.

Particle morphology, atomic composition were conducted by transmission electron microscopy (TEM, Jeol 2100F 200kV) equipped with an EDS. EDX analysis was also obtained on carbon coated Cu grids. SEM images were controlled to collect the data for the size-distribution charts by analyzing 50 NP for the metal borate samples and plotting with respect to their frequencies (Philips XL 30S FEG). SEM samples were prepared on carbon tapes by providing a drop from the corresponding EtOH solutions. In order to avoid the electron charging effect, samples were coated with 5 nm Au prior to the SEM imaging. FT-IR spectra were analyzed by dried nanoparticles in between 400 cm^{-1} -4000 cm^{-1} with Agilent 600 series ATR module Spectrophotometer. Thermal properties of the synthesized particles were analyzed between room temperature and 1000 $^{\circ}\text{C}$ with 20 $^{\circ}\text{C}/\text{min}$ increasing rate under N_2 atmosphere by TGA Shimadzu DTG-60 series. UV-Vis absorption properties of the nanoparticles in EtOH dispersion were conducted by UV-Vis Spectrophotometer in between 200-800 nm with Agilent Cary 60 UV-Vis Spectrophotometer. Surface properties and atomic composition of metal borate nanostructures were investigated by XPS spectroscopy. XPS spectrums have been obtained by a flood gun charge neutralizer system equipped with a monochromatic Al K α X-ray source ($h\nu=1486.6 \text{ eV}$) from 400 mm spot size on the nanoparticles. Wide energy survey scans have been recorded between 0–1360 eV binding energy range, at detector pass energy of 200 eV and with energy step size of 1 eV. High resolution spectra were obtained at pass energy of 50 eV and with energy steps of 0.1 eV for each atom.

The antibacterial activity of silver borate, copper borate and zinc borate nanoparticles were tested against Gram-positive *Staphylococcus aureus* (ATCC 6538) and Gram-negative *Escherichia coli* (ATCC 25922). Activation of ATCC cultures were done by storing at $-80 \text{ }^{\circ}\text{C}$, and plantations into petri-plants with Nutrient Agar (Merck) was realized. Muller Hinton Broth (MHB) (Merck), was utilized to for bacterial counts by the "dilution method". Nutrient Broth (NB) (Merck) was is the environment for the bacterial growth procedure. Incubation at $37 \text{ }^{\circ}\text{C}$ was conducted during 24 h, and suspensions were set to 0.5 McFarland turbidity with sterile PBS.

Crystallinity of the metal borate NP's

Crystallinity and phases of the silver, copper and zinc borate nanoparticles investigated by XRD. In Fig. 2a, 2b, 2c and 2d all the peaks were analyzed according to the varying mole ratios at $90 \text{ }^{\circ}\text{C}$. This means, silver and borax ratios were kept stable with 4 different applications. In Fig. 2a Ag/borax ratio was 1/2 and it is easily seen that increasing temperature forms a very high crystallinity. Fig. 2b and Fig. 2c show that if the ratio was changed to 1/1.5 and 1/1 formation of the silver borate at low temperatures are very sensitive and especially 1/1.5 has a very low crystallinity. Still when the silver ratio increases to 2 versus borax 1, as in Fig. 2d, quite a perfect crystal structures are observed. (Fig 2d) unveils the XRD patterns of

as-synthesized silver borate particles. Obtained patterns are highly similar with hexagonal silver borate crystals with JCPDS: 96-150-9895 number. Bragg reflections with 2θ measurements were showed below;

30.00° , 33.20° , 33.79° , 34.19° , 38.04° , 39.21° , 43.33° , 44.21° , 48.99° , 52.66° , 55.77° , 60.56° , 64.31° , 66.61° and 77.32° . Corresponding peaks are detectable for silver borate structures as 33.2° , 38.5° , 55.6° and 66.1° which is for AgB_4 and AgB_3 .

When XRD patterns of copper borate are examined with typical XRD pattern of copper borate nanoparticles at 90°C , formation is related to the presence of Cu/borax ratio and independent from the temperature (Fig. 3a, 3b, 3c and 3d). It is seen that the highest intensity of the copper borate formation occurs when the Cu / Borax mole ratio is 2/1. Examination of the patterns revealed that increasing the proportion of the copper lowers the peak intensities (Fig. 3d). It can be stated that the formation of copper borate doesn't occur unless the molar ratios are proper like 2 / 1 Cu/borax. According the these result; at Fig. 3d molar ratios for Cu/borax is 2/1 which is ideal for the copper borate particle formation. Possibly molecular geometry for metal borate structure provides thermodynamic stability on these proportions.

Standart JCPDS: 96-210-5419 number and peak list was detected. Different detected Bragg values with 2θ angles of 23.90° , 29.51° , 34.50° , 39.06° , 42.4° and 48.04° were observed. It is seen that the highest intensity of the copper borate formation occurs when the Cu / Borax mole ratio is 2/1. Increasing copper mol amounts revealed decreased XRD peak intensity of the as-synthesized particles (Fig. 3e).

When XRD patterns of zinc borate are examined with typical XRD pattern of synthesized zinc borate nanoparticles in Fig. 4a, 4b, 4c and 4d. The peaks were analyzed according to the different mole ratios at 90°C . Fig. 4a, 4b and 4c Zn/borax ratio was 1/2, 1/1.5 and 1/1 respectively and it is easily seen that at 90°C forms a very high crystallinity.

When the zinc ratio increases to 2 versus borax 1, as in Fig. 4d, quite a perfect crystal structures are observed. (Fig. 4e) are the XRD peaks of zinc borate structures which may be attributed to JCPDS: 96-720-4694 number. Bragg reflections and also 2θ measurements of 22.10° , 28.10° , 33.50° , 36.30° , 37.20° , 42.90° and 65.90° were detected.

Morphology and Atomic Characterization

TEM investigations of the as-synthesized metal borate nanostructures were completed for the size, atomic structure and morphology detection. Results unveiled that obtained structures are in the nanorange with complex size and morphology features.

Overview images of the TEM investigation were presented in Figure 5. Investigation showed that nanostructures of the as-synthesized metal borate particles are in the nanometer scale. Since relatively high agglomeration is occurred in the nanoparticles seen in SEM images, TEM provides clearer insight to the fabricated nanoparticles. Interestingly silver borate structures are nearly spherical and there is no other impurities observed. B1-b2 images represent the copper borate nanostructures where generally plate

like structures were observed. Zinc borates (c1-c2) are elongated and show irregular size distribution. For the statistical size distribution morphologies and distribution range calculation is only possible for the silver borate nanostructures since particle sizes are in a small distribution range where numerical detection is possible with graphical plot. Silver borate nanoparticles are in the 15-30 nm range and show high crystallinity. Nanoparticles are nearly spherical but size variations cause irregular comparison among the nanoparticles. Small agglomerations are visible but do not change the primary character of the nanoparticles from the compact structure formation perspective. Particles are separate and possibly organic agglomerations form darker regions on carbon coated Cu grid. Interestingly copper borate nanoparticles show 2D like morphology. Plate like geometry is observed and size ranges lie between 300-500 nm. Detected particles showed that copper borate morphology do not carry organic pollutants on the surface but nanoparticle thickness is great enough form a single compact structure. Since size and geometry of the nanoparticles affect the antibacterial feature of the materials, this 2D structure should be highlighted and evaluated accordingly. Zinc borate nanostructures are rod like materials. Diameters of these rod like structures are between 50-100 nm range. Additionally broken and irregular shapes are also visible. TEM investigation of the metal borate structures clearly confirm that as-synthesized particles are in the nanorange. Even though their dense agglomerations are detected in SEM images, fine structures observed by TEM, confirm that size range is in the nanoregime.

From the XRD characterization we have concluded that morphological examination is also necessary for the nanoparticle investigation. Therefore we have utilized the solutions of silver borate (AgB13), copper borate (CuB13) and zinc borate (ZnB13) for morphological and appearance investigation. Nanoparticles shapes and their magnitudes were detected by SEM and atomic compositions were obtained using EDX. Measurements were done by a drop of dispersed solution of EtOH. Drops were placed on carbon tape and surface coated with 5 nm Au to increase the imaging quality.

In the examination, it was seen that AgB13 (Fig. 6a and 6b) nanoparticles are spherical, CuB13 (Fig. 6c and 6d) and ZnB13 (Fig. 6e and 6f) are plate-shaped and there is no other impurities in the products. For AgB13 spherical particles, it was observed that in some particles inner sides of the spheres are empty and particle distribution is presenting a narrow range. Also it was detected that particles are relatively large but less in number. With increasing scale, larger particles get more noticeable.

SEM measurements revealed that as-synthesized particle size for AgB13 particles was an average of 321 nm. The particle sizes of CuB13 particles were determined to be 754 nm on average. The dimensions of the particles can be imagined as two dimensional and the layer thicknesses were measured between 150-200 nm.

In the measurements of the synthesized ZnB13 particles from the SEM image, it was determined that the two dimensional thicknesses ranged from 210 nm to 280 nm (Supporting Fig. 1).

As stated and confirmed by TEM before, silver, copper and borate structures show different morphologies. When we compared the crystallinity and morphology it is easier to detect the sample nanoparticle which we can use for the further applications.

EDX revealed the atomic character of the nanoparticles by revealing Ag, Cu, Zn, B and O element ranges detected by the available composition (Supporting Fig. 2). This investigation clearly shows the three metal borate formation with high purity. Calculated atomic proportions were also showed as insert table pictures on EDX graphs.

Surface Characterization with FT-IR and XPS Analysis

FTIR investigation of the nanoparticle surfaces for AgB13, CuB13 and Zn13 were presented at (Supporting Fig. 3). Conducted FT-IR analysis on dried nanoparticles shown that intense peaks at 890 and 1350 cm^{-1} are due to the B-O stretching of $\text{B}_4\text{-O}$ and $\text{B}_3\text{-O}$. Also 510-590 cm^{-1} peaks can be attributed to the B-O-B linkages [30]. FT-IR analysis also revealed that surface of the particles show -OH peaks which may belong to water in crystalline structure. Copper borate structure shows a doublet at around 1250 cm^{-1} which differentiate its spectra from the other zinc and silver borate structures. Silver borate show a large and intensive peak at fingerprint region when compared to others. Especially the band at 1600 cm^{-1} is accepted as H-O-H bending since this value can be attributed to the crystalline water. Related other peaks such as 3400 cm^{-1} is also belongs O-H stretching. Also the band between 3250-3500 cm^{-1} additionally confirms the O-H group and H-O-H bond. Additionally the band in the fingerprint region, 1350-1252 cm^{-1} shows the band B-O bonding, while the band between 1089-983 cm^{-1} shows the asymmetric $\text{B}_4\text{-O}$ bonding. Peak at 942-866 cm^{-1} shows the $\text{B}_3\text{-O}$ peak and the band at 782-730 cm^{-1} reveals the symmetrical $\text{B}_3\text{-O}$ stretch [31].

Survey XPS also clearly indicates the presence of all atoms together with C and Na peaks (Fig. 7a). In Fig. 7b Ag 3d peaks centered at 367.88 and 373.68 eV for Ag 3d_{5/2} and Ag 3d_{3/2} observed [32]. B atoms 1s peak is seen at 189 eV and can be accepted as B-OH. Additional peaks at 188 eV and 186 eV for the B-O and Ag-O-B respectively [33]. Therefore B atoms 1s peaks for AgB13 confirm the peak at 186 eV indicates the boron element in the sample (Fig. 7c). The band in AgB13 can be accepted for substitution of boron element into the Oxygen in AgB13 lattice and hybrid B(2p) and O(2p) orbitals [34]. For the O 1s peaks in (Fig. 17d) 530.38 eV was due to hydroxyl groups while the peak at 527 eV belongs to borate group.

The BE at 530.38 eV for O 1s peak confirms the B₂O₃ structure, consistent with the B 1s peak at 189.98 eV of oxygen bonded boron structure [35].

As for the CuB13, Survey XPS also clearly indicates the presence of all atoms together with C and Na peaks (Fig. 8a). Cu 2p peaks in Fig. 8b confirms the Copper element by two peaks positioned at 931.08 eV and 958.38 eV which means the Cu 2p_{3/2} and Cu 2p_{1/2} orbitals. Peaks for the CuB13 structure has symmetrical shape with satellite peaks. Two satellite peaks were detected as bigger energy value for Cu 2p peaks [32-36]. B 1s core spectra shows the main peak positions at 192 eV due to boron-oxo species in Fig. 8c. The component at 190 eV is associated with the B-O state and the last at 191 eV is associated with Cu-O-B. Peak of B1s for CuB13 confirms the availability of boron at 186 eV validating boron element [37]. Fig. 8d is the O 1s peak of CuB13 structure.

Detailed investigation of the O 1s peak unveils that symmetrical shape of the O 1s peak is

clearly seen meaning one type of oxygen sites in CuB 13 structure. Therefore, O 1s spectrum was detected that –OH and B-O is available [35].

Survey XPS of ZnB13 clearly indicates the presence of all atoms together with C and Na peaks (Fig. 9a). Zn 2p core level spectrum in Fig. 9b represent one peak located at 1022.03 eV confirming the Zn 2p_{3/2} and unveils the deconvoluted Zn 2p_{3/2} peak. Lower energy peak (1022.3 eV) is accepted as ZnO [37]. B atoms 1s peak is positioned at 192 eV possibly because of the B-O species in Fig. 9c. The component at 190 eV is associated with the B-O state and the last at 191 eV is associated with Zn-O-B. Peak of the B atoms 1s for ZnB13 unveiled a peak at 186 eV confirms the B atom in ZnB13 [37]. Fig. 9d is the O atoms 1s orbital peak for ZnB13 sample.

Investigations showed that it is easy to detect O 1s spectra and its shape showing one of the oxygen roles in ZnB 13 structure. Therefore, O 1s spectrum was detected and deeply investigated [35]. Results unveiled that –OH type and B-O type oxygen types are visible.

Thermal and Optical Properties of Nanoparticles

TG–DTA profiles of the obtained and selected silver borate, copper borate and zinc borate structures were presented at Fig. 10, 11 and 12 respectively. From the graphical investigation during thermal application, we have detected that volatile parts are water.

For silver borate nanoparticles (AgB13), 12.70 wt% loss with three temperatures 185.27 °C, 376.32 °C and 483.82 °C were detected. (Fig. 10a and 10b). Investigation was realized starting from room temperature to 1000 °C. Total crystal water was detected and amount was calculated as 12 % corresponding $\text{Ag}_2\text{O}\cdot 2\text{B}_2\text{O}_3\cdot 3\text{H}_2\text{O}$ formula. Silver Borate structure has loss before 200 °C, which also allows the calculation of the volatile molecules on $\text{Ag}_2\text{O}\cdot 2\text{B}_2\text{O}_3\cdot 3\text{H}_2\text{O}$. At 185 °C and 485 °C, crystal water is detected.

For copper borate nanoparticles (CuB13), amount of the thermal loss is 40.51 wt% and this happens at 260.73 °C. Temperature has started from the room conditions and ended at 1000 °C which can be compared with total water amount in the crystal. From calculations 40.51 % was found and formulation was presented as $\text{CuO}\cdot 2\text{B}_2\text{O}_3\cdot 8\text{H}_2\text{O}$ (Fig. 11a and 11b). Copper Borate crystals have loss at 260 °C which can be linked to the absorbed water and other volatile molecule decomposition. Additionally endothermic loss at 260 °C possibly corresponds to molecular water. For zinc borate nanoparticles, (ZnB13) loss is 13.35 wt% at 494.83 °C. For zinc borate particles total loss was detected as 13.35 % corresponding $\text{ZnO}\cdot 2\text{B}_2\text{O}_3\cdot 2\text{H}_2\text{O}$ structure (Fig. 12a and 12b). Beginning weight loss is at 200 °C, and endothermic sign between 493 °C and 594 °C, is attributed to the crystal water.

UV Vis graphic of the silver borate (AgB13), copper borate (CuB13) and zinc borate (ZnB13) nanostructures were scanned between 200 and 800 wavelength nm in EtOH solutions which is shown at

Supporting Fig. 4. Maximum absorption is generally seen at 230-420 nm. Size of the particles play an important role. Since surface can contain water or –OH groups there is no absorption is detected after 400 nm. All particles showed except CuB13 were well dispersed but CuB13 shows agglomerations where also supported by SEM images.

Antibacterial Investigation for Nanoparticle Embedded Ceramic Glazes

It is widely known that particles and their sizes are directly effecting the melting behaviour, surface roughness and appearance of glazes. Since obtained nanoparticle sizes have varying values, different glaze compositions were obtained with different amounts of metal borate nanoparticles (Figure 13). Generally glaze surfaces are treated like easy to clean surfaces but different sources of pitting or degradations diminishes the glaze features. It is possible that glaze may contain different crystalline phases in addition to the glassy phase for controllable properties. From this viewpoint introduced metal borate nanoparticles can affect the durability, corrosion resistance, chemical resistance and antibacterial character with specially added agents. Metal borate nanoparticles were dispersed in industrial glaze formulations to obtained metal borate doped glaze structures showing antibacterial characteristics. Since blank particle-free ceramic glazes showed no detectable antibacterial effect, source of this antipathogen activity is due to the metal borate nanoparticles. Ceramic glazes were produced with varying amounts of nanoparticles embedded (0,25%, 0,5% 1%, 2%, 3%, 4% (w/w) of metal borate structures (Supporting Fig. 5). Particles were dispersed in this glazing composition at 500 rpm for 15 minutes then raw ceramic surfaces were coated. Obtained ceramic composition was kept at 1200 °C during 12 hours. In order to detect the antipathogenic character, ceramic glazes were kept in 121 °C and 1 atm for 15 minutes. Additionally 50 ml centrifuge tubes which was cleaned in 70% ethanol and bacterial suspension (10^7 CFU ml^{-1}) was introduced to tubes and incubated at 37 °C in a shaking incubator at 100 rpm for 24 hours. Then bacterial suspension produced from the samples was repeatedly diluted and put into the agar medium by having 0.1 ml of the sample. Then bacterial colonies were detected after incubation for 24 hours at 37 °C.

Antibacterial measurements were compared with reference ceramic glazes containing any of the metal borate nanoparticles and labeled as blank. Antibacterial measurements were detected by the formula below [38].

$$\text{Antibacterial activity (\%)} = (A-B) / A \times 100$$

A is accepted as control sample, and B is the columns taken from the nanomaterials inoculation.

(Fig.14a-h) showed antibacterial feature against *S. aureus* and *E. coli* bacteria. According to

the results, 1% AgB 13 containing ceramic composition showed the highest antibacterial effect against *S. aureus* and *E. coli* bacteria when compared to 0,25% and 0,5% AgB13. It seems 0,25% and 0,5% AgB13 do not show the antibacterial effect. Therefore amount of the silver borate nanoparticles was increased to 1% in the ceramic glaze. Results showed that *S. aureus* and *E. coli* bacteria were 100% reduced with 1%

AgB13 particle containing ceramic glaze formulation. It is seen that ceramics containing CuB13 provide full protection against *S. aureus* but does not provide a full protection against *E. coli* bacteria (Fig.15a-h). Therefore, in order to increase the antibacterial effect of the copper borate nanoparticle embedded glazes, 2% CuB13 was utilized against *S. aureus* bacteria and interestingly %100 protection was detected (Fig. 15d).

Unexpectedly same amount of the copper borate nanoparticles against to *E. coli* bacteria showed only 85% inhibition. Hence, it is possible to reveal that CuB13 structure is selectively effective on Gr+ *S. aureus*. More interestingly 3% CuB13 unfortunately caused the ceramic

formation problems during the high temperature application. Also ceramic glazes containing ZnB13 provided different antibacterial feature when tested against to *S. aureus* and *E. coli* bacteria (Fig.16a-h). Amount of the zinc borate nanoparticles were 4% to obtain %100 antibacterial feature (Fig. 16d and h). Consequently when compared to each other; 1% AgB13 and 4% ZnB13 nanoparticles show 100 % effectivity against to Gr+ and Gr- bacteria while 2% of CuB13 shows selective antibacterial effect against to Gr+ bacteria. However 2% copper borate nanoparticle inhibition against to Gr- bacteria is about 85% and 3% CuB13 is not allowing the formation of a standard ceramic glaze causing unexpected cracks on the surface.

Conclusions

Detailed investigations clearly showed that silver, copper and zinc borate nanoparticles possessing the antibacterial features with varying morphologies and sizes obtained. During the physical and chemical analysis together with the surface investigation, particle morphology, optical and thermal properties were detected. TEM, SEM with EDX investigations in addition to XRD measurements revealed that purity of the as-synthesized particles are clear and shapes are varying. XPS results were also showed the clear formation of the metal borates with clear boron peak positions. The antibacterial features against to gram positive and gram negative bacteria were tested for industrial ceramic glazes. When compared unadditive standart ceramics showed no antibacterial feature while 1% AgB13 and %4 ZnB13 show perfect antibacterial activity. Interestingly 2% CuB13 showed perfect antibacterial effect against Gr+ bacteria but only 85% inhibition against to Gr- was observed. As a conclusion it was shown that metal borate nanostructures were mechanistically investigated and utilized as antibacterial agent in ceramic industry implying a proper material for the similar applications.

Declarations

Conflicts of interest

The authors declare no conflicts of interest.

Acknowledgements

We acknowledge Manisa Celal Bayar University Coordination Unit For Scientific Research Projects (BAP) (Project No: 2014 – 152) and İstanbul Sabahattin Zaim University Halal Food Laboratories for analytic investigations and also NOS Keskin for antibacterial tests.

References

1. Hamelian M, Zangeneh MM, Shahmohammadi A, Varmira K, Veisi H (2020) Pistacia atlantica leaf extract mediated synthesis of silver nanoparticles and their antioxidant, cytotoxicity, and antibacterial effects under in vitro condition. *Appl Organometal Chem* 34:e5278. <https://doi.org/10.1002/aoc.5278>
2. Dhanwe VP, Joshi PG, Kshirsagar AS, Dhapte VV, Khanna PK, *ChemistrySelect* 2018, 3, 7548
3. Zhang C, Liu J, Ahmeda A et al. Biosynthesis of zinc nanoparticles using *Allium saralicum* R.M. Fritsch leaf extract; Chemical characterization and analysis of their cytotoxicity, antioxidant, antibacterial, antifungal, and cutaneous wound healing properties. *Appl Organomet Chem*. 2020;e5564. <https://doi.org/10.1002/aoc.5564>
4. Ibrahim NA, Eid BM, Abou Elmaaty TM, El-Aziz EA (2013) A smart approach to add antibacterial functionality to cellulosic pigment prints. *Carbohydr Polym* 94:612–618
5. Wei A, Yao Y, Wang T, Shen L, Jia L, Chen S (2018) Decoration of Ag nanoparticles on the apatite nanosheet-coated silica nanofibers with enhanced anti-bacterial property and photo-catalytic activity. *Mater Lett* 230:236–240. <https://doi.org/10.1016/j.matlet.2018.07.129>
6. Hoseinnejad M, Jafari SM, Katouzian I (2018) Inorganic and metal nanoparticles and their antimicrobial activity in food packaging applications. *Crit Rev Microbiol* 44:161–181. <https://doi:10.1080/1040841X.2017.1332001>
7. Chernousova S, Epple M (2013) Silver as Antibacterial Agent: Ion, Nanoparticle, and Metal. *Angewandte Chemie Int Ed* 52:1636–1653. <https://doi.org/10.1002/anie.201205923>
8. Gustafson L,, Chew,, Markham,, Bell,, Wyllie, and Warmington (1998) Effects of tea tree oil on *Escherichia coli*. *Lett Appl Microbiol* 26:194–198. doi:10.1046/j.1472-765X.1998.00317.x
9. Ağuş O, Abalı Y, Arslan O, San Keskin NO, Facile and controlled production of silver borate nanoparticles, *SN Applied Sciences*, (2019), 1:662. <https://doi.org/10.1007/s42452-019-0686-y>
10. Camello T, Souza M, Martins C, Damasco P, Marques E, Pimenta F, Pereira G, Hirata R Jr, Mattos-Guaraldi A (2009) *Corynebacterium pseudodiphtheriticum* isolated from relevant clinical sites of infection: a human pathogen overlooked in emerging countries. *Lett Appl Microbiol* 48:458–464. doi:10.1111/j.1472-765X.2009.02553.x
11. Hajipour MJ, Fromm KM, Akbar Ashkarran A, Jimenez de Aberasturi D, de Larramendi IR, Rojo T, Serpooshan V, Parak WJ, Mahmoudi M (2012) Antibacterial properties of nanoparticles. *Trends Biotechnol* 30:499–511. <https://doi:10.1016/j.tibtech.2012.06.004>

12. Tuomela S, Autio R, Buerki-Thurnherr T, Arslan O, Kunzmann A, Andersson-Willman B, Wick P, Mathur S, Scheynius A, Krug HF, Fadeel B, Lahesmaa R (2013) Gene Expression Profiling of Immune-Competent Human Cells Exposed to Engineered Zinc Oxide or Titanium Dioxide Nanoparticles. *PLoS One* 8(7):e68415. doi:10.1371/journal.pone.0068415 Published online 2013 Jul 22.
13. Arslan O, Uyar T (2017) Multifunctional electrospun polymeric nanofibrous mats for catalytic reduction, photocatalysis and sensing. *Nanoscale* 9(27):9606–9614
14. Anjum S, Singh S, Benedicte L, Roger P, Panigrahi M, Gupta B, *Global Challenges* 2018, 2, 1700068. <https://doi.org/10.1002/gch2.201700068>
15. Raghupathi KR, Koodali RT, Manna AC (2011) Size-dependent bacterial growth inhibition and mechanism of antibacterial activity of zinc oxide nanoparticles. *Langmuir* 27:4020–4028. <https://doi:10.1021/la104825u>
16. Nitschke M, Araújo L, Costa S, Pires R, Zeraik A, Fernandes A, Freire D, Contiero J (2009) Surfactin reduces the adhesion of food-borne pathogenic bacteria to solid surfaces. *Lett Appl Microbiol* 49:241–247. doi:10.1111/j.1472-765X.2009.02646.x
17. Buerki-Thurnherr T, Xiao L, Diener L, Arslan O, Hirsch C, Maeder-Althaus X, Grieder K, Wampfler B, Mathur S, Wick P, Harald F, Krug (2013) In vitro mechanistic study towards a better understanding of ZnO nanoparticle toxicity. *Nanotoxicology* 7:4. DOI:10.3109/17435390.2012.666575 402–416
18. Parham S, Wicaksono DHB, Bagherbaigi S, Lee SL, Nur H (2016) Antimicrobial Treatment of Different Metal Oxide Nanoparticles: A Critical Review. *J Chinese Chem Soc* 63:385–393. <https://doi:10.1002/jccs.201500446>
19. Arslan O, Belkoura L (2015) Swift synthesis, functionalization and phase-transfer studies of ultrastable, visible light emitting oleate@ ZnO quantum dots. *J Mater Chem C* 3:1965–1973
20. Arslan O, Aadesh SP, Belkoura L, Mathur S (2013) Cysteine modified Zwitterionic ZnO Quantum Dots. *J Mater Res* 28(14):1947–1954
21. Kim SH, Lee S, In I, Park SY (2016) Synthesis and antibacterial activity of surface-coated catechol-conjugated polymer with silver nanoparticles on versatile substrate. *Surf Interface Anal* 48:995–1001. doi:10.1002/sia.6004
22. Ciacotich N, Kragh KN, Lichtenberg M, Tesdorpf JE, Bjarnsholt T, Gram L (2019) In Situ Monitoring of the Antibacterial Activity of a Copper–Silver Alloy Using Confocal Laser Scanning Microscopy and pH Microsensors. *Global Challenges* 3:1900044. <https://doi.org/10.1002/gch2.201900044>
23. Arslan O, Arpac E, Sayilkan H (2010) Siliconcarbide embedded hybrid nanocomposites as abrasion resistant coating. *J Inorg Organomet Polym Mater* 20(2):284–292
24. Tang S, Zheng J (2018) *Adv Healthcare Mater* 7:1701503. <https://doi.org/10.1002/adhm.201701503>
25. Laga M, Meheus A, Piot P (1989) Epidemiology and control of gonococcal ophthalmia neonatorum. *Bull World Health Org* 67:471–477
26. Saint S, Elmore JG, Sullivan SD, Emerson SS, Koepsell TD (1998) The efficacy of silver alloy-coated urinary catheters in preventing urinary tract infection: a metaanalysis. *Am J Med* 105:236–241

27. Sudha VBP, Ganesan S, Pazhani GP, Ramamurthy T, Nair GB, Venkatasubramanian P (2012) Storing drinking-water in copper pots kills contaminating diarrhoeagenic bacteria. *J Health Popul Nutr* 30:17–21
28. Arslan O, Arpaç E, Sayılkan F, Sayılkan H (2007) Hybrid sol–gel coating on Al. *J Mater Sci* 42(6):2138–2142
29. Shvarts EM, Belousova RG (2006) Formation of Tricuprotetrateborate $3\text{CuO}\cdot 2\text{B}_2\text{O}_3\cdot 6\text{H}_2\text{O}$ in Aqueous Solutions. *Russ J Appl Chem* 79(4):672–673
30. Dimitriev Y, Bachvarova-Nedelcheva A, Iordanova R, Glass formation tendency in the system $\text{SeO}_2\text{-Ag}_2\text{O-B}_2\text{O}_3$, *Mater Res Bull* 43 (2008) 1905–1910 <https://doi.org/10.1016/j.materresbull.2007.06.054>
31. Gao X, Guo Y, Tian Y, Li S, Zhou S, Wang Z (2011) Synthesis and characterization of polyurethane/zinc borate nanocomposites. *Colloids Surfaces A: Physicochemical Engineering Aspects* 384:2–8
32. Selvarajan S, Suganthi A, Rajarajan M (2018) A novel highly selective and sensitive detection of serotonin based on Ag/polypyrrole/ Cu_2O nanocomposite modified glassy carbon electrode. *Ultrason Sonochem.* <https://doi.org/10.1016/j.ultsonch.2018.02.038>
33. Singh Surah S, Vishwakarma M, Kumar R, Nain R, Sirohi S, Kumar G (2019) Tuning the electronic band alignment properties of TiO_2 nanotubes by boron doping. *Results in Physics* 12:1725–1731. <https://doi.org/10.1016/j.rinp.2019.01.081>
34. Wang S, Bian C, Jia B, Wang Y, Jing X (2016) Structure and thermal pyrolysis mechanism of poly(resorcinol borate) with high char yield. *Polym Degrad Stab* 130:328e337. <http://dx.doi.org/10.1016/j.polymdegradstab.2016.06.006>
35. Sung J, Shin M, Deshmukh PR, Hyun HS, Sohn Y, Shin WG (2018) Preparation of ultrathin TiO_2 coating on boron particles by thermal chemical vapor deposition and their oxidation-resistance performance. *J Alloy Compd* 767:924e931. <https://doi.org/10.1016/j.jallcom.2018.07.152>
36. Khattak GD, Mekki A, Gondal MA (2010) Effect of laser irradiation on the structure and valence states of copper in Cu-phosphate glass by XPS studies. *Appl Surf Sci* 256:3630–3635. <https://doi.org/10.1016/j.apsusc.2009.12.167>
37. Zhang W, Yang B, Chen J, Effect of calcination temperature on preparation of boron-doped TiO_2 by sol-gel method, *International Journal of Photoenergy* (2012), Article ID: 528637. <https://doi.org/10.1155/2012/528637>
38. San Keskin NO, Kiliç NK, Dönmez G, Tekinay T (2016) Green synthesis of silver nanoparticles using cyanobacteria and evaluation of their photocatalytic and antimicrobial activity. *J Nano Res* 40:12

Figures

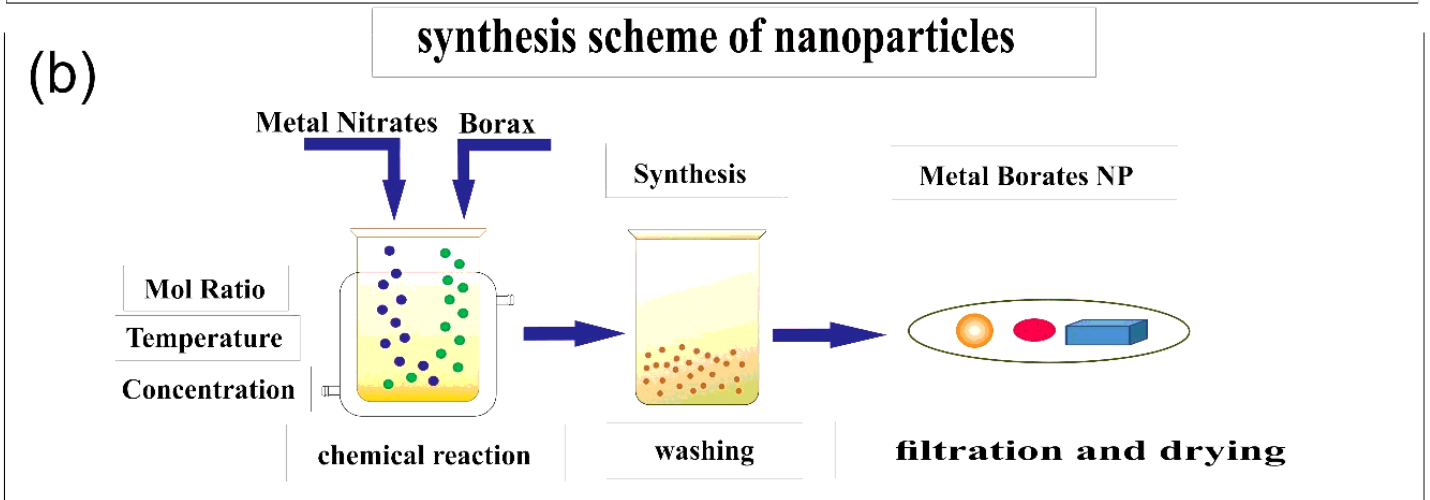
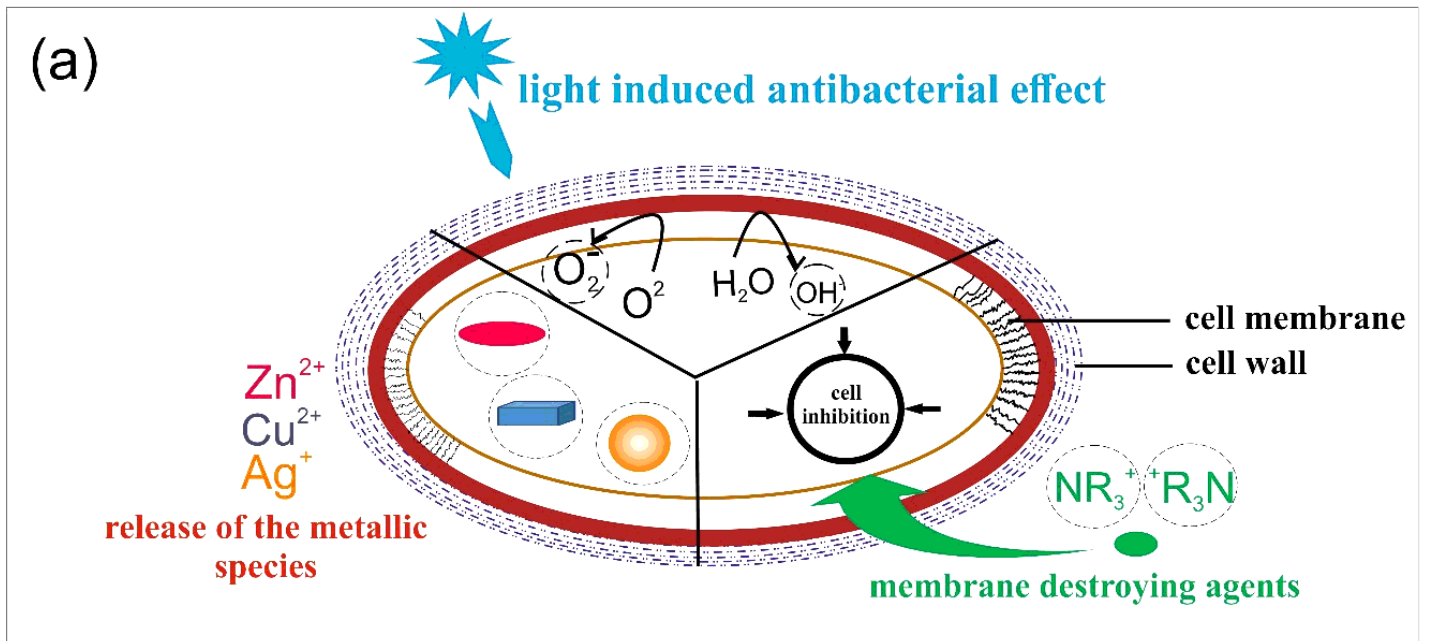


Figure 1

Affecting antibacterial mechanisms and active methods with synthesis method of metal borate nanoparticles

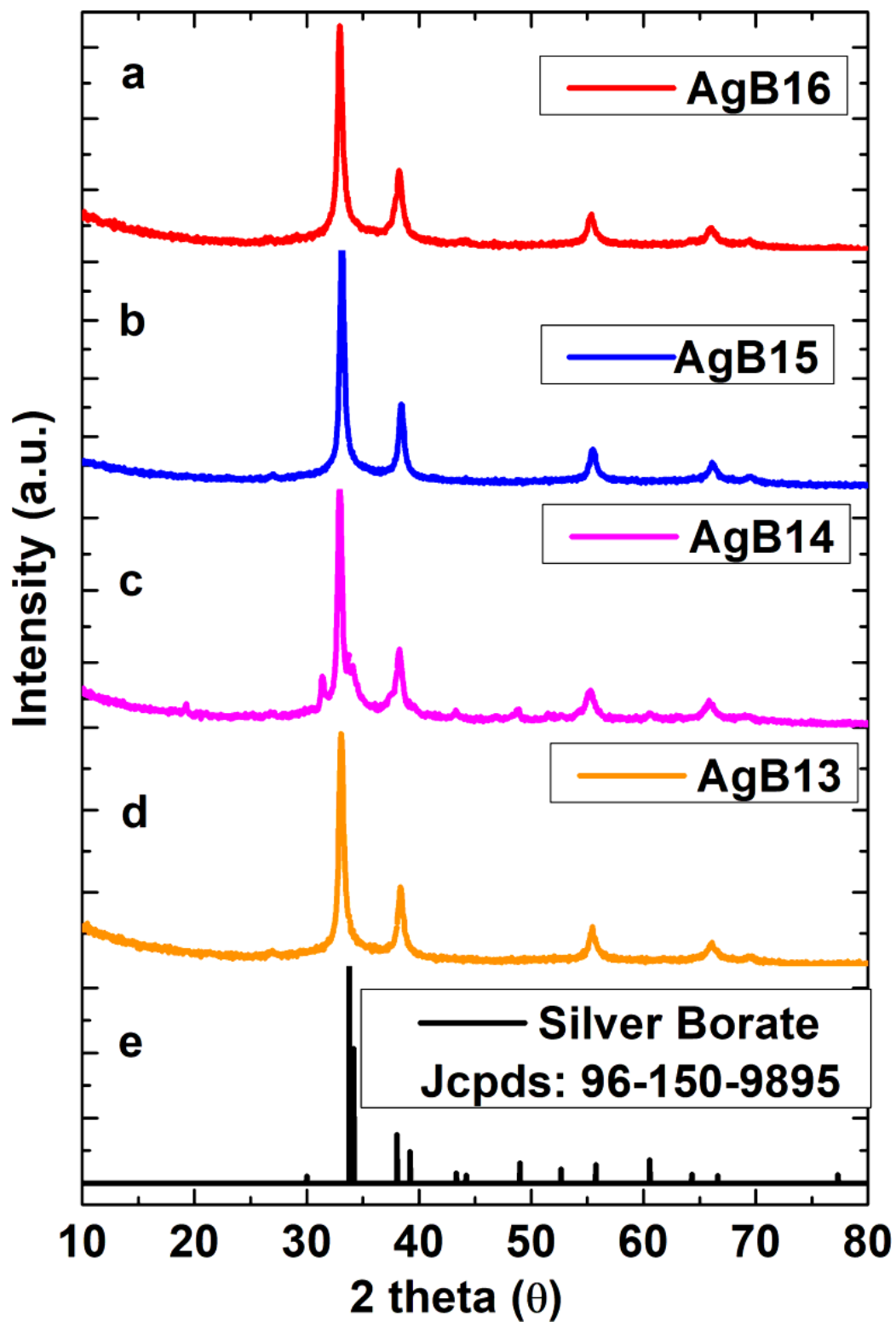


Figure 2

Formation of Silver Borate at 90 °C a) mole ratios Silver/Borax at 1/2, b) mole ratios Silver/Borax at 1/1.5 c) mole ratios Silver/Borax at 1/1, d) mole ratios Silver/Borax at 2/1, e) Comparison of the synthesized AgB with JCPDS: 96-150-9895 peaks.

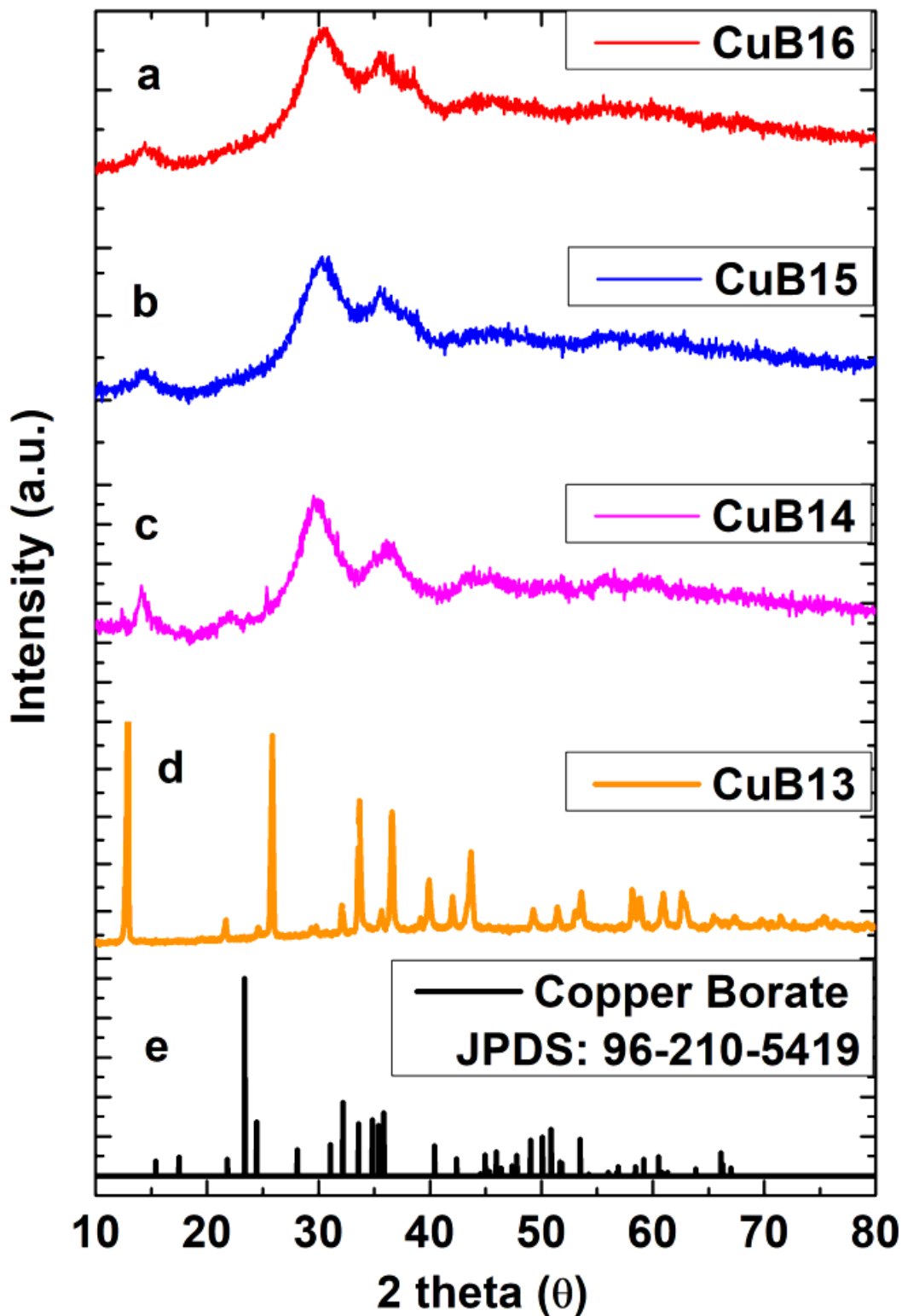


Figure 3

Formation of Copper Borate at 90 °C a) mole ratios Copper/Borax at 1/2, b) mole ratios Copper /Borax at 1/1.5 c) mole ratios Copper /Borax at 1/1, d) mole ratios Copper /Borax at 2/1, e) Comparison of the synthesized CuB with JCPDS: 96-210-5419 peaks.

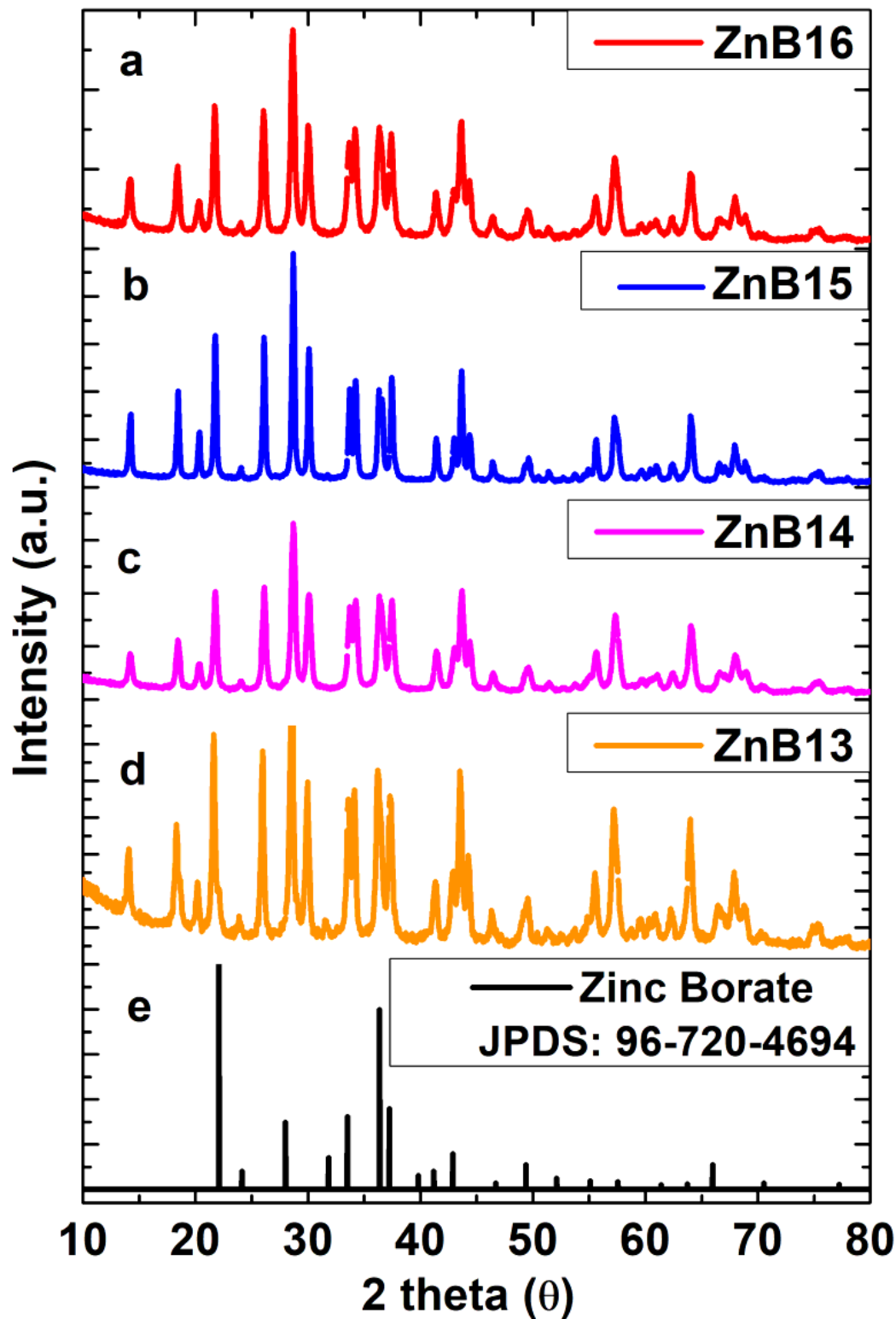


Figure 4

Formation of Zinc Borate at 90 °C a) mole ratios Zinc/Borax at 1/2, b) mole ratios Zinc /Borax at 1/1.5 c) mole ratios Zinc /Borax at 1/1, d) mole ratios Zinc/Borax at 2/1, e) Comparison of the synthesized ZnB with JCPDS: 96-720-4694 peaks.

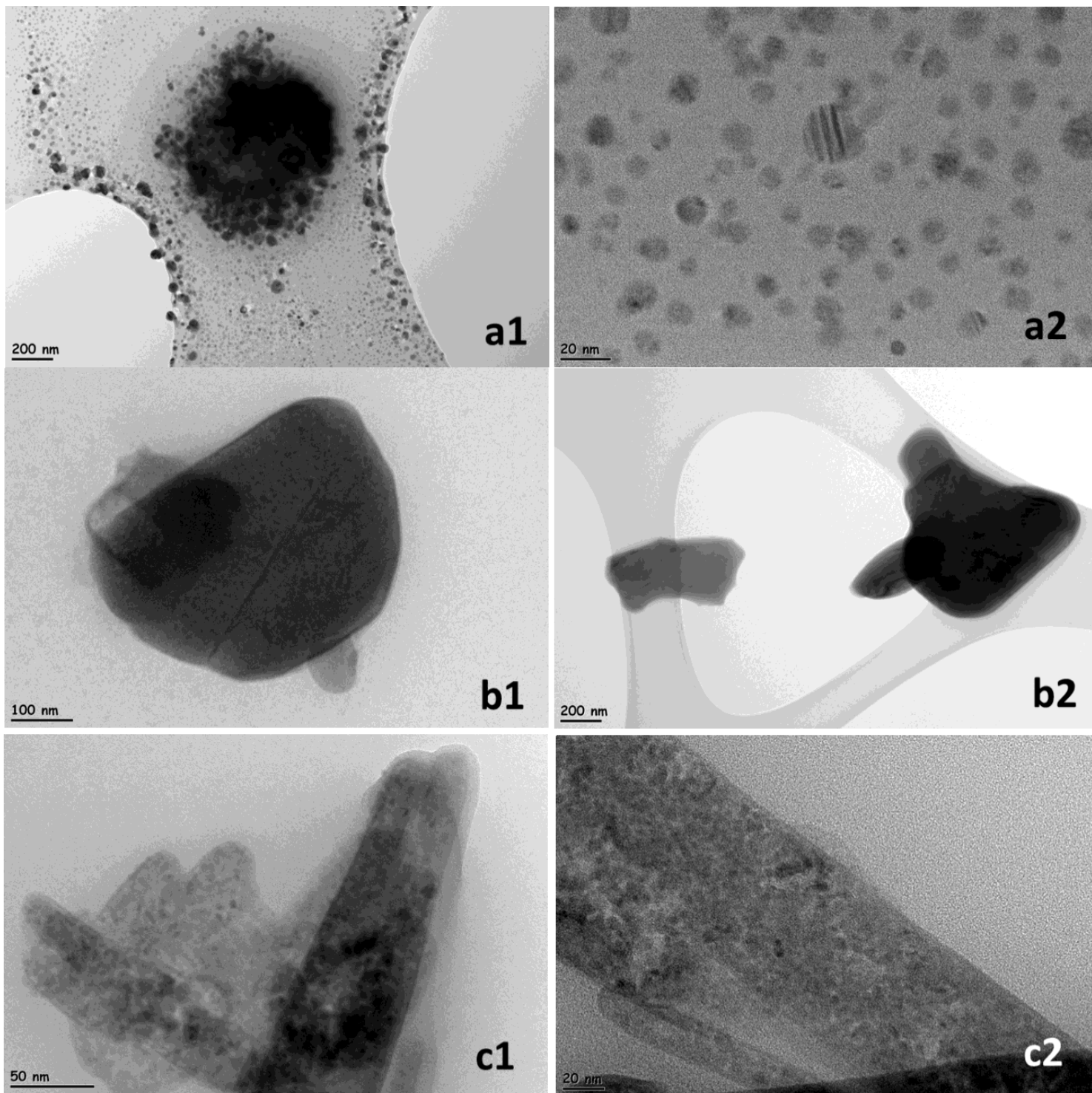


Figure 5

TEM investigation of the as-synthesized metal borate nanoparticles; silver borate (a1-a2), copper borate (b1-b2), zinc borate (c1-c2)

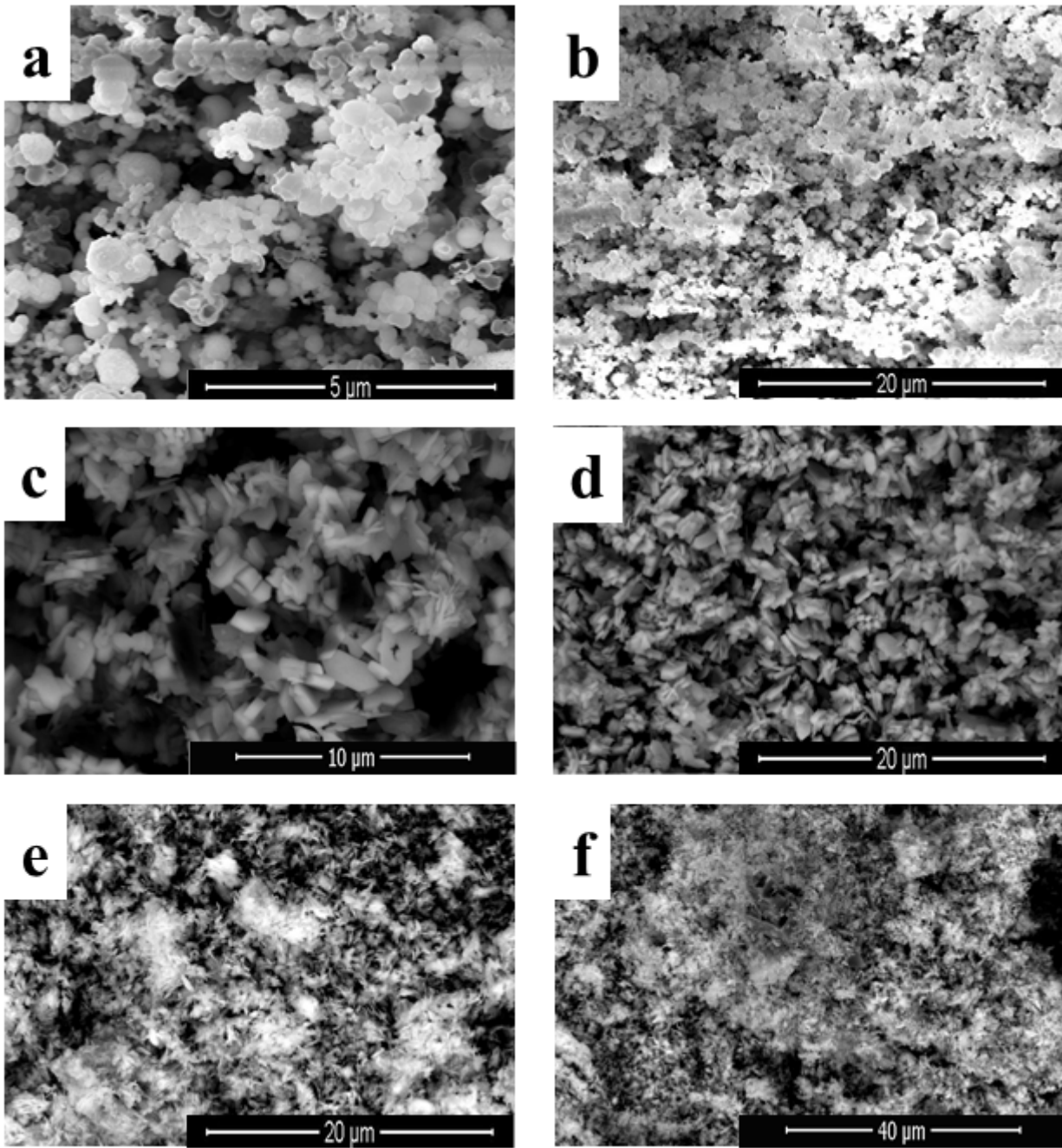


Figure 6

Representative SEM images of the a) AgB13 at 5 μm b) AgB13 at 20 μm c) CuB13 at 10 μm d) CuB13 at 20 μm e) ZnB13 at 20 μm f) ZnB13 at 40 μm magnification values

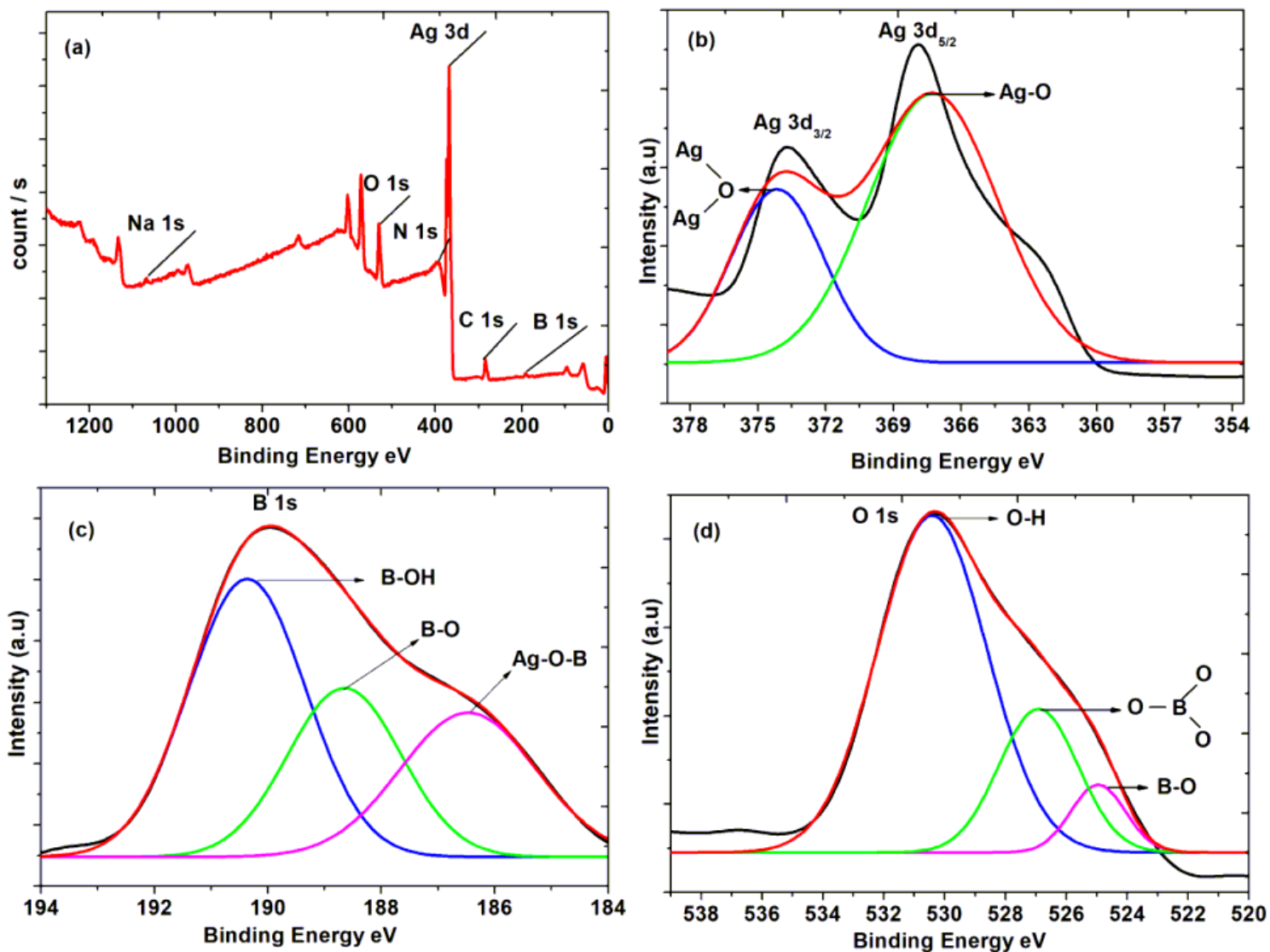


Figure 7

The XPS spectra a) AgB13 survey b) Ag3d core spectra c) B1s core spectra d) O1s core spectra of the sample AgB13

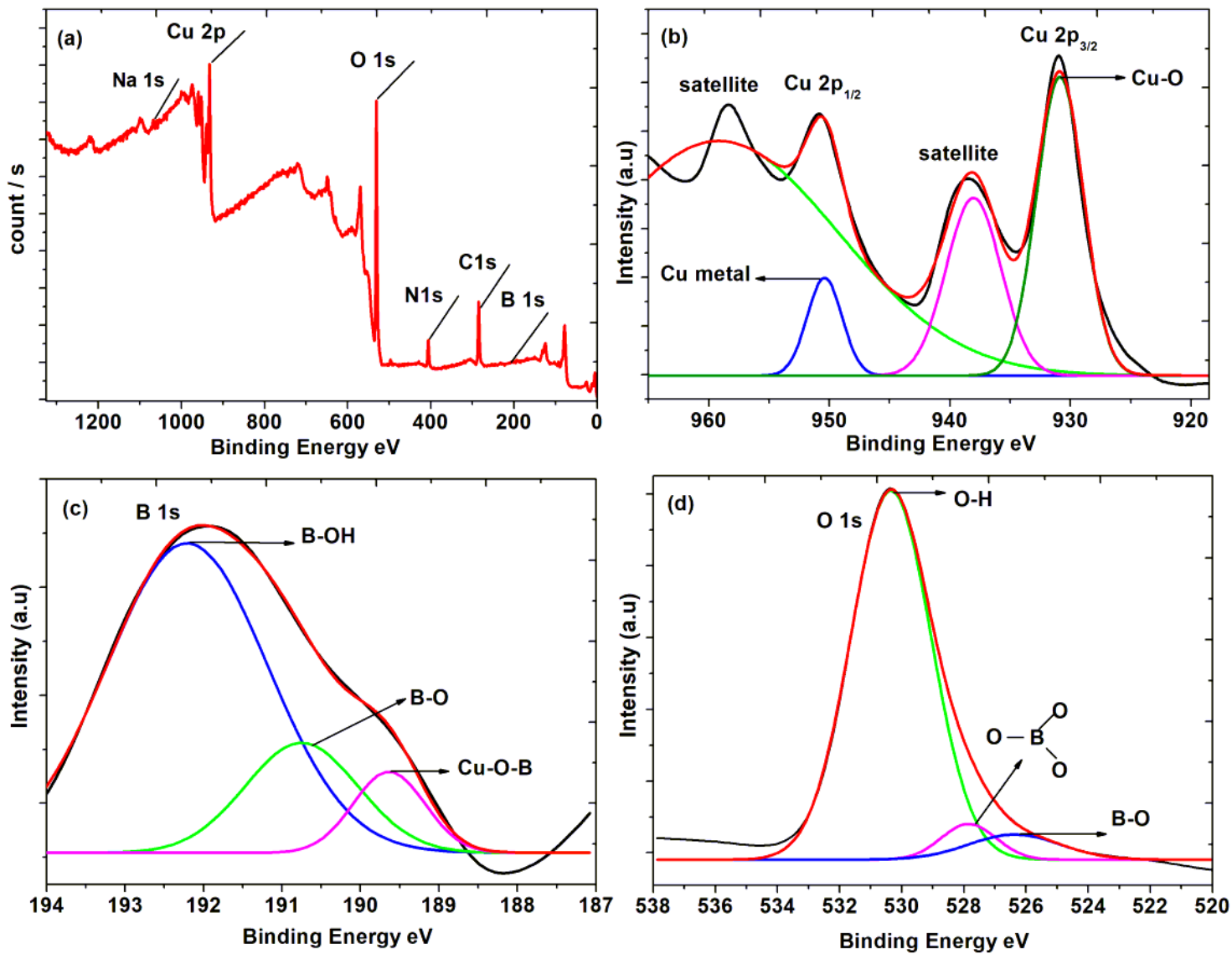


Figure 8

The XPS spectra a) CuB13 survey b) Cu 2p peak c) B 1s peak d) O 1s peak of CuB13

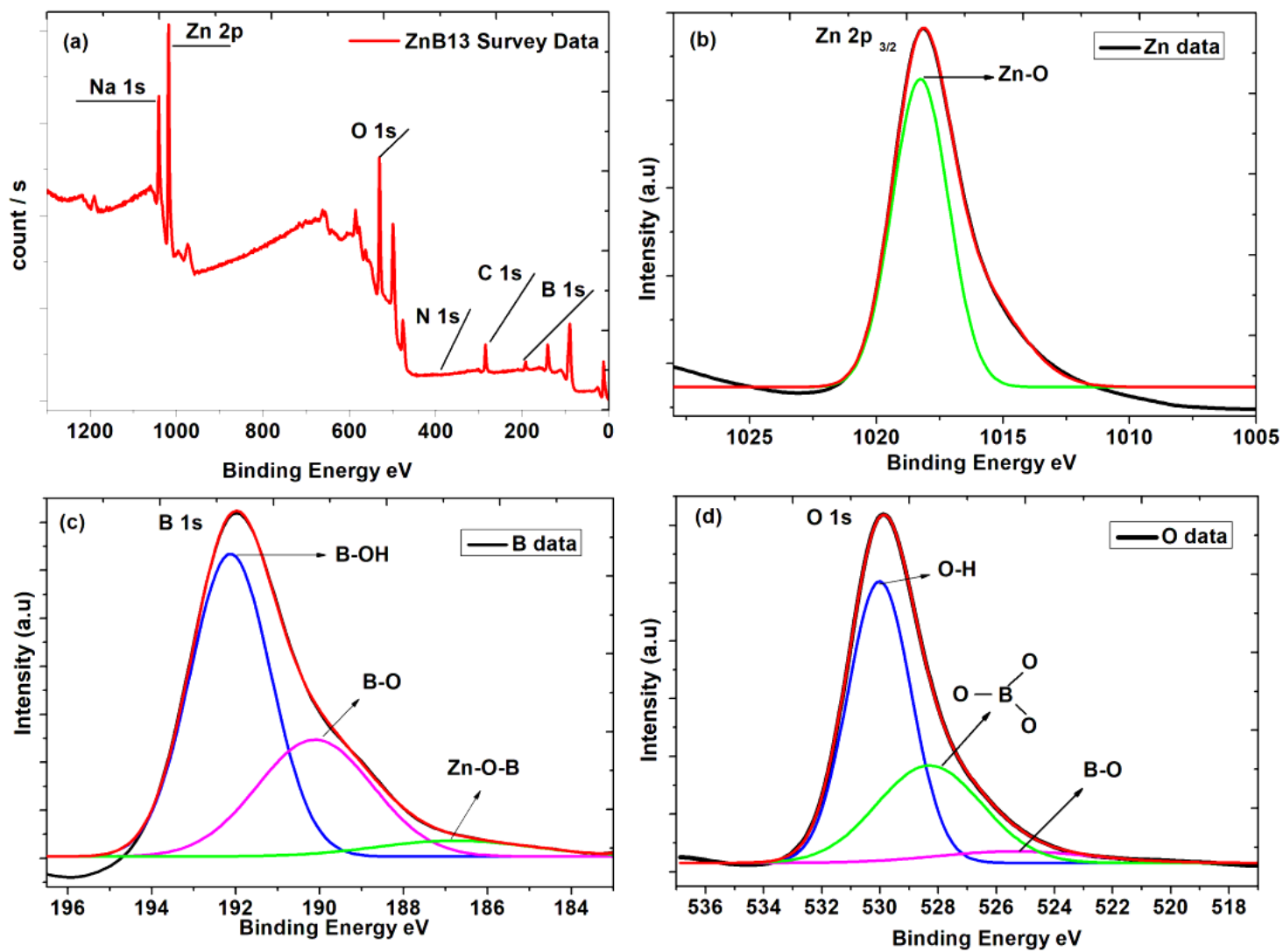


Figure 9

The XPS spectra a) ZnB13 survey b) Zn 2p core spectra c) B1s core spectra d) O1s core spectra of the sample ZnB13

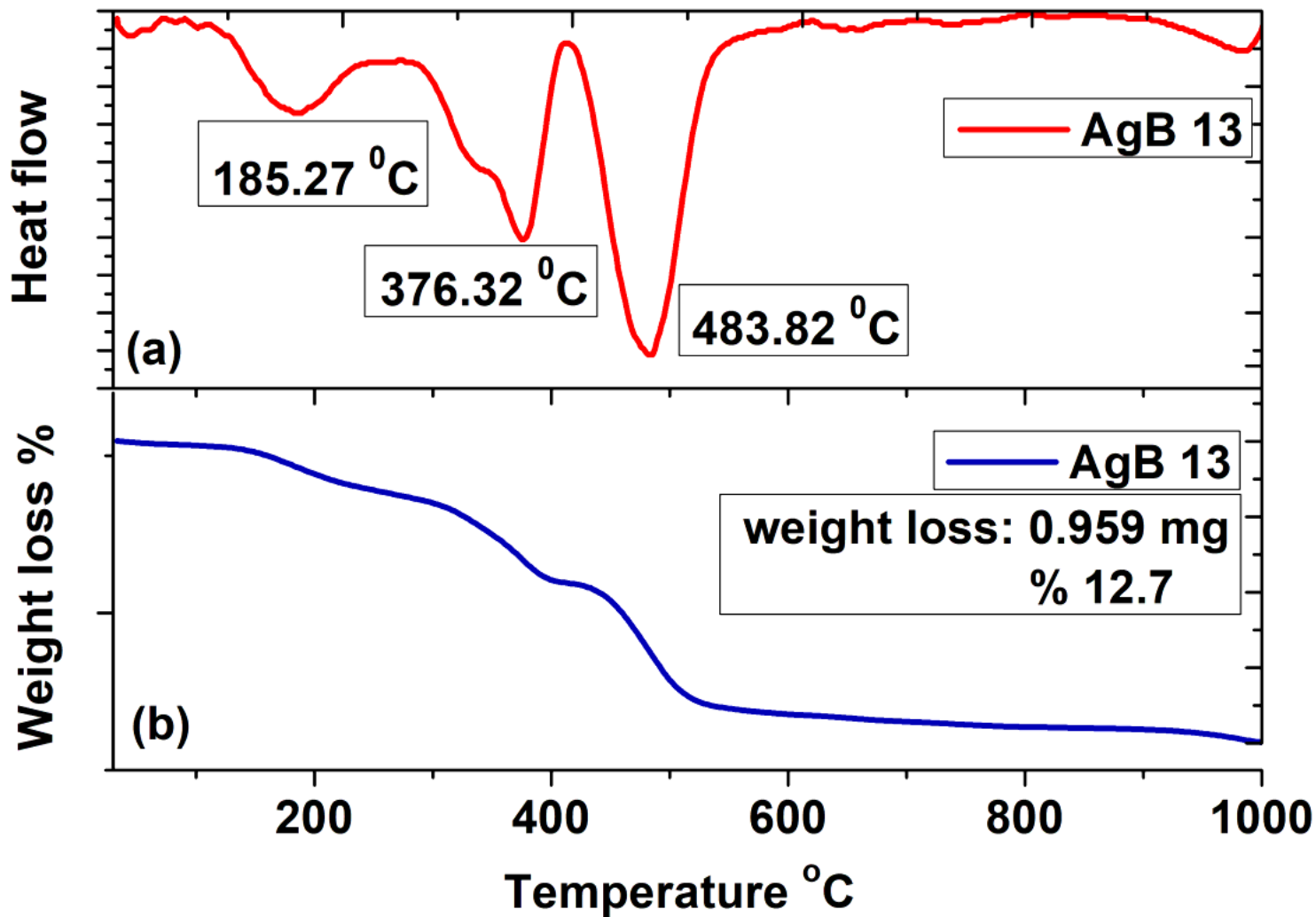


Figure 10

a) AgB13 DTA graph, b) TGA analysis of AgB13

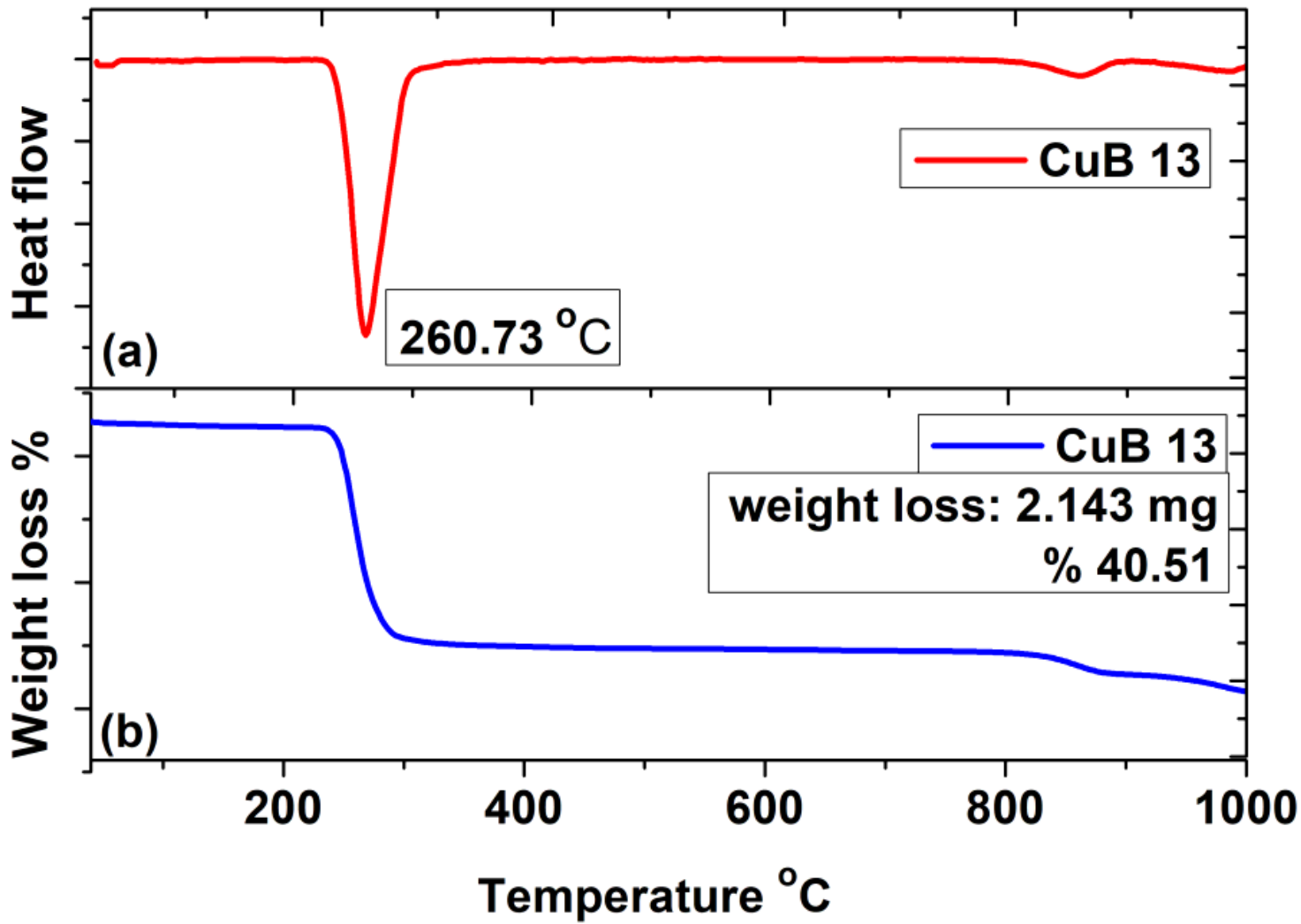


Figure 11

a) CuB13 DTA graph, b) TGA analysis of CuB13

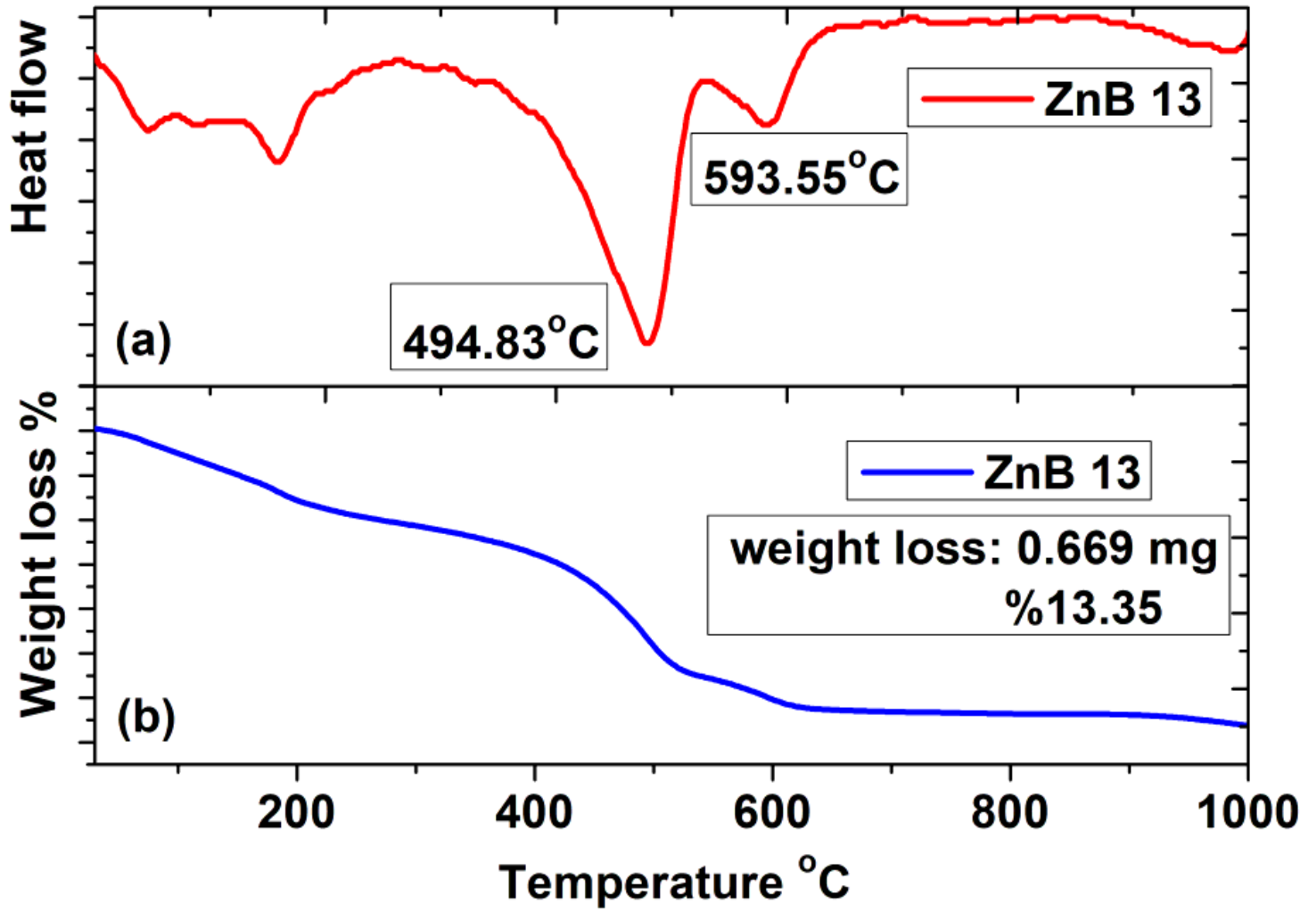


Figure 12

a) ZnB13 DTA graph, b) TGA analysis of ZnB13

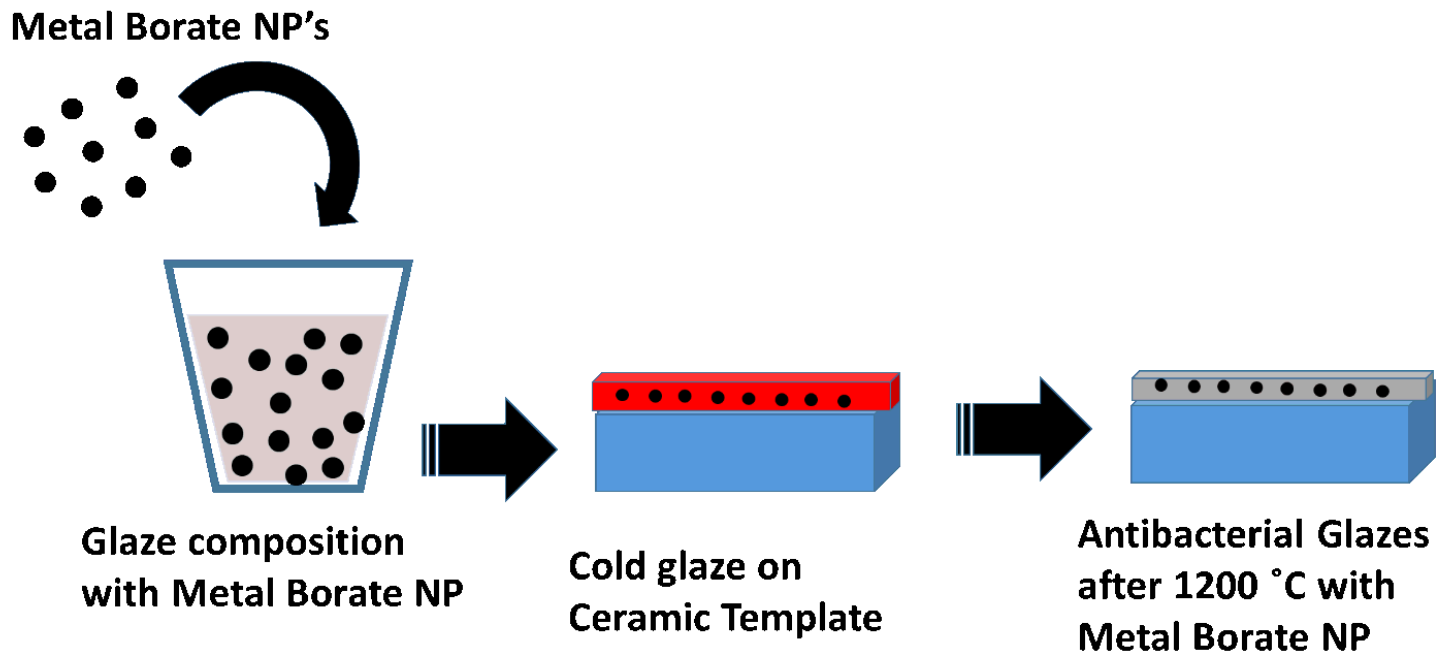
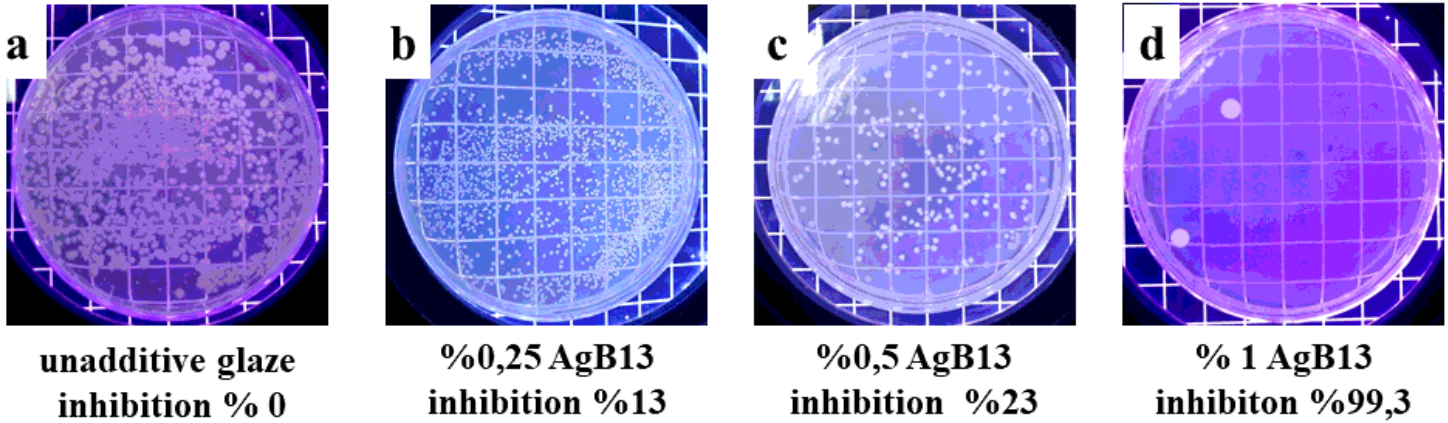


Figure 13

Process for the metal borate NP embedded antibacterial galze formation

Gram-positive *Staphylococcus aureus* (ATCC 6538)



Gram-negative *Escherichia coli* (ATCC 25922)

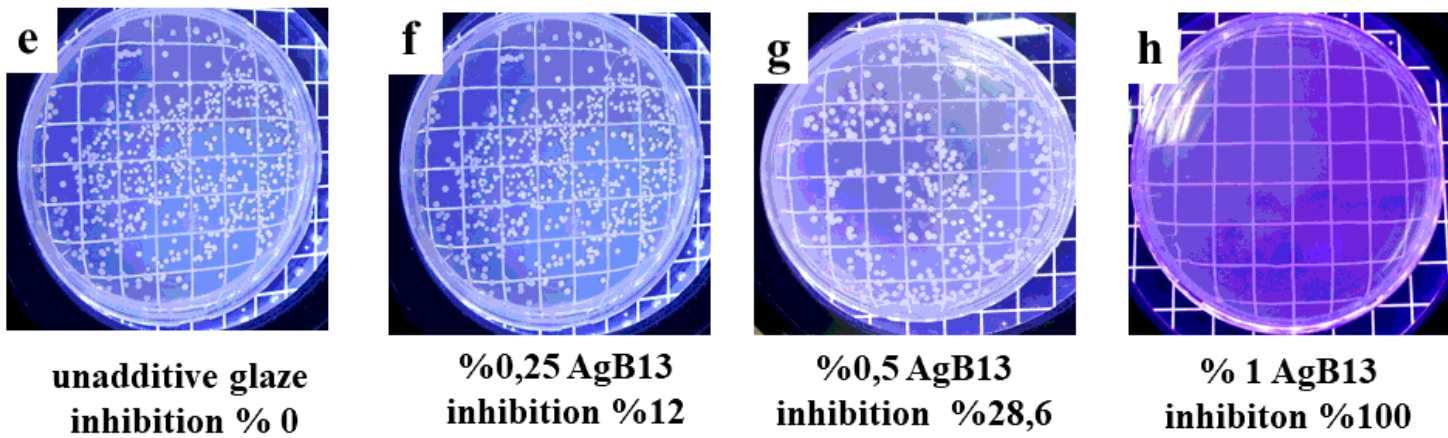
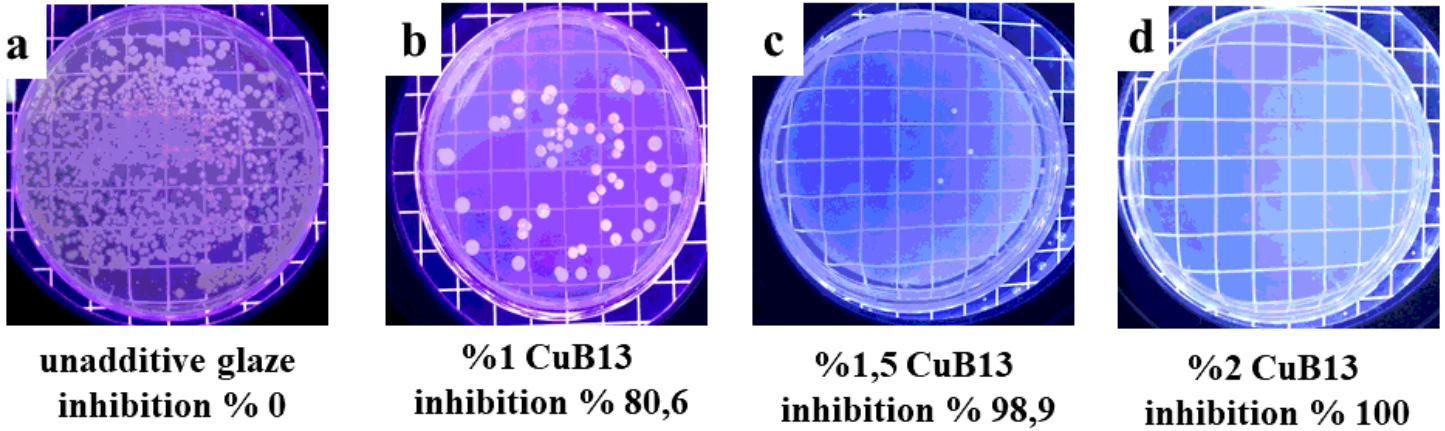


Figure 14

Antibacterial test results of silver borate (AgB13) nanoparticles against *Staphylococcus aureus* a) unadditive glaze b) 0,25 % AgB13, c) 0,5 % AgB13, d) 1 % AgB13 against *Escherichia coli* e) unadditive glaze f) 0,25 % AgB13, g) 0,5 % AgB13, h) 1 % AgB13

Gram-positive *Staphylococcus aureus* (ATCC 6538)



Gram-negative *Escherichia coli* (ATCC 25922)

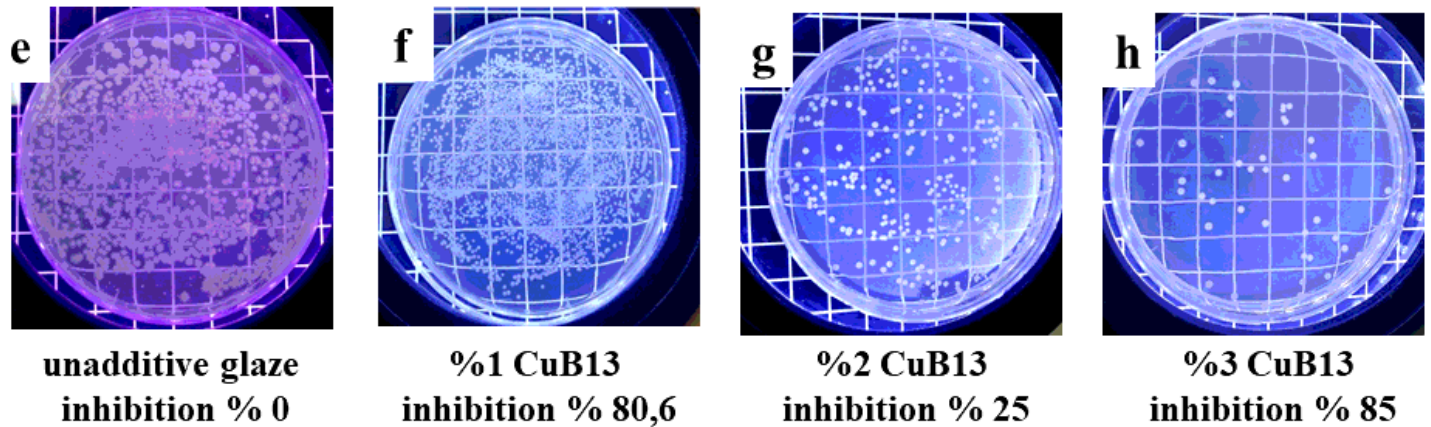
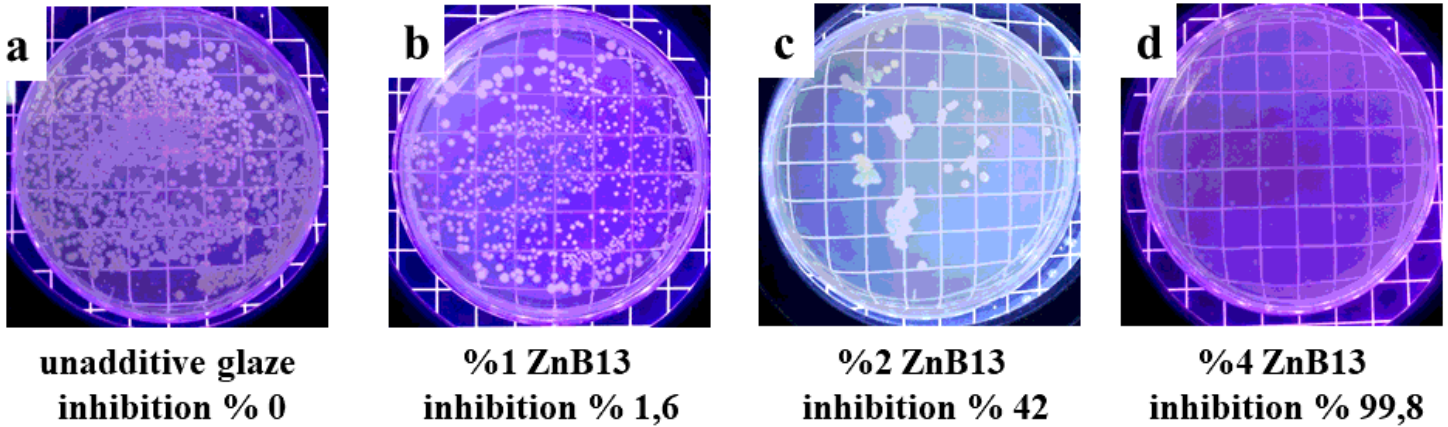


Figure 15

Antibacterial test results of copper borate (CuB13) nanoparticles againsts *Staphylococcus aureus* a) unadditive glaze b) 1 % CuB13, c) 1,5 % CuB13, d) 2 % CuB13 against *Escherichia coli* e) unadditive glaze f) 1 % CuB13, g) 1,5 % CuB13, h) 2 % CuB13

Gram-positive *Staphylococcus aureus* (ATCC 6538)



Gram-negative *Escherichia coli* (ATCC 25922)

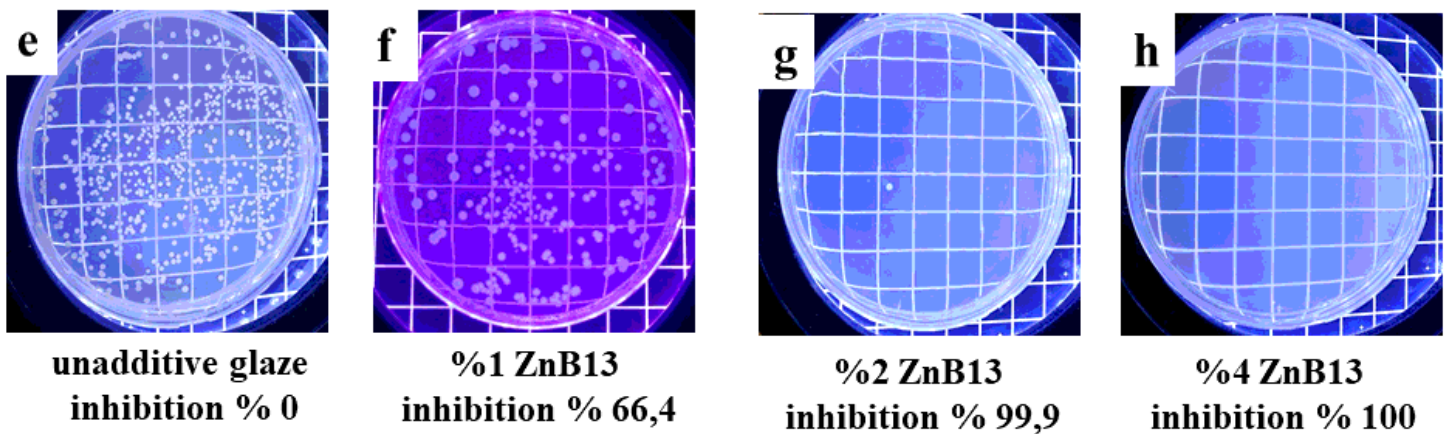


Figure 16

Antibacterial test results of zinc borate (ZnB13) nanoparticles against *Staphylococcus aureus* a) unadditive glaze b) 1 % ZnB13, c) 2 % ZnB13, d) 4 % ZnB13 against *Escherichia coli* e) unadditive glaze f) 1 % ZnB13, g) 2 % ZnB13, h) 4 % ZnB13

Supplementary Files

This is a list of supplementary files associated with this preprint. Click to download.

- [SupportingInformation.docx](#)